Asymptotically Efficient Estimator for Range-based Robot Relative Localization

Yue Wang, Muhan Lin, Xinyi Xie, Yuan Gao, Fuqin Deng, and Tin Lun Lam†

***Abstract*—This study investigates the 2D relative localization problem, which estimates the relative orientation and position between two moving robots using inter-robot range measurements. We propose a novel formulation and a robust weighted semidefinite relaxation solution for the relative localization problem in the presence of range measurement error and robot state transition error. Theoretical analysis and simulations show that the weighted semidefinite relaxation solution achieves CRLB performance when the measurement noise and the odometry uncertainty follow Gaussian distributions with moderate noise power. Demonstrations using data from a laboratory environment validate the promising and robust performance of the weighted semidefinite relaxation method. The root-mean-square errors in estimating the orientation and position are 3.97^o and 0.22 meters with affordable hardware.**

I. Introduction

Determining the pose of an agent is one of the fundamental tasks of a robotic system [1], [2]. Robotic systems relying on a global positioning system [3] are not suitable for the indoor environment. The absolute pose of a robot with respect to the global frame is inaccessible without external information [4], [5], [6], which restricts a robotic system's application and operation range. Robot relative localization determines the robot's relative pose [7], which refers to the position and orientation of a robot seen from the viewpoint of a reference robot, using local measurements.

In recent years, the study of robot relative localization has gotten more attention because it is crucial for target interception/surrounding [8], robot swarming [9], and micro aerial vehicles system [10], [11]. Camera, lidar, and RGB-D scanner are several sensor options for robot localization and navigation. However, many reconfigurable modular robots are self-assemblable and small, such as FreeBot [12] and magnetically controlled modular cubes [13]. The view of the visual sensor could be limited because of flipping or blocking. Tagging information indicates to which robots the measurements refer (data association problem). The untagged data can be identified using the unsupervised clustering method [14], [15] or treated as the input of a mutual localization problem with anonymous measurements [16], [17]. The range measurements collected by ultra-wideband (UWB) modules are fully registered, thus avoiding the data association problem. Moreover, the UWB-based method is desirable because of its low cost, low power consumption, high accuracy, and ability to operate in a non-line-of-sight environment [18]. In addition to the UWB module, our approach assumes that the mobile robots are equipped with inertial measurement units (IMUs) or two-wheel differential-type odometers to measure the translation and rotation of the mobile robot with respect to its body frame. The lightweight and affordability of the UWB module and the odometer enable the deployment of a group of small, inexpensive robots in a GPS-denied environment.

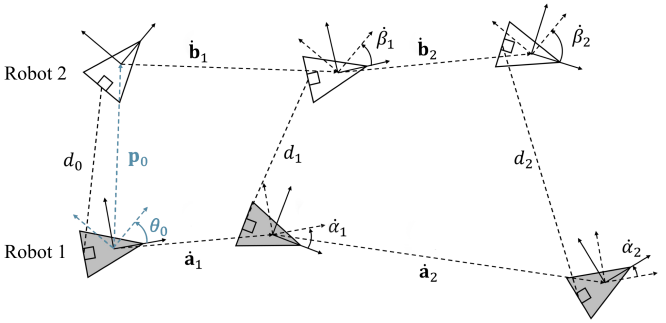

Fig. 1. Scenario of robot relative localization. The gray triangles and white triangles represent the trajectories of Robot 1 and Robot 2. The squares indicate the UWB modules. We aim to determine the orientation and the position of Robot 2 under Robot 1's frame at the initial moment, i.e., θ_0 and $\mathbf{p}_0$.

Sensor network-based rigid body localization (RBL) is closely related to robot relative localization problems. For RBL, anchors are placed at known global positions around a rigid body. Range or bearing measurements between sensors mounted on the rigid body and known anchors are exploited to instantaneously estimate the global pose of a rigid body [19], [20]. However, the average noise magnitude of range measurements obtained by UWB modules is about 0.1 meters, which is in the same order of magnitude as the size of many modular robots. Determining the robot's relative pose instantaneously using the measurements collected in a single frame has a high chance of failure because of the sensor array aperture limitation of small robots. Alternatively, using odometry and range measurements from different time instances instead of placing multiple sensors on a robot saves the implementation cost and significantly expands the array aperture.

This work was supported by the National Natural Science Foundation of China (62073274), and the funding AC01202101103 from the Shenzhen Institute of Artificial Intelligence and Robotics for Society. (†Corresponding author: Tin Lun Lam, email: tllam@cuhk.edu.cn)

Yue Wang and Yuan Gao are with the Shenzhen Institute of Artificial Intelligence and Robotics for Society, Shenzhen, 518000, China (e-mail: ericawang@cuhk.edu.cn, gaoyuan@cuhk.edu.cn).

Muhan Lin and Xinyi Xie are with the Chinese University of Hong Kong, Shenzhen, 518172, China (e-mail: 119010177@link.cuhk.edu.cn, 120040057@link.cuhk.edu.cn).

Fuqin Deng is with the Wuyi University, School of Intelligent Manufacturing, Jiangmen, 529020, China, and also with the Shenzhen Institute of Artificial Intelligence and Robotics for Society, Shenzhen, 518000, China (e-mail: dengfuqin@cuhk.edu.cn).

Tin Lun Lam is with School of Science and Engineering, the Chinese University of Hong Kong, Shenzhen, 518172, China, and also with the Shenzhen Institute of Artificial Intelligence and Robotics for Society, Shenzhen, 518000, China (e-mail:tllam@cuhk.edu.cn).

Many relative localization approaches are only interested in the relative position of the robots. Mourikis et al. [21] investigate the maximum expected positioning uncertainty of heterogeneous robotic teams as a function of the parameters such as 1) the size of the robot group; 2) the accuracy of the sensors; and 3) the topology of the RPMG, i.e., the weighted directed graph representing the network of robot-to-robot exteroceptive measurements. Güler et al. [22] propose an onboard robot relative localization framework to determine tag robots' position and heading using the mixture Monte Carlo localization estimator. The base robot in [22] is mounted with three UWB modules, which may exceed the size and power limitations of the mobile robot. [23]. Shalaby et al. [23] design a multi-agent system containing two-tag agents. 3D relative positions for any number of agents are attainable with at least two two-tag agents. Agents in [23] equip with the attitude and heading reference system (AHRS) consisting of an accelerometer, a gyroscope, and a magnetometer to measure the global orientation information in the North-East-Down (NED) coordinate. On the other hand, an IMU only measures the local orientation information with respect to its body frame. However, the AHRS requires careful calibration [24], and the accuracy of the magnetometer is affected by electromagnetic interference.

If the trajectory of the target in the frame of the reference robot is available, the general Procrustes analysis aligns the target trajectory in its own frame with the target trajectory in the reference frame and solves the coordinate transformation between the target frame and the reference frame. Determining the target trajectory can be viewed as a Euclidean distance matrix (EDM) completion problem [25]. The diagonal block and the diagonal elements of the off-diagonal block of the EDM are known. Pocholska et al. [26] reconstruct polynomial/bandlimited target trajectories based on the odometry information of the reference robot and inter-robot range measurements.

Several existing studies are designed to determine the relative pose between two robots at the initial moment, which is the same task as this study. Zhou et al. [27] propose an algebraic 2D robot relative pose estimation method followed by a weighted least square refinement. Further, Zhou et al. [27] analyze the condition when the unique solution exists, as well as the observability based on the Lie derivatives. In [28], [29], Zhou et al. investigate the problem of 3D robot relative localization using the minimal number of the range and bearing measurements. The relative localization problem comprises 14 minimal systems with multiple solutions. Outlier rejection schemes such as Random Sample Consensus (RANSAC) are applied to reject the incorrect solutions and identify the most proper inlier set. However, the bearing sensors are typically more expensive than the UWB module, and the outlier rejection method is computationally intensive when more measurements are involved. Trawny et al. [30] solve the first-order optimality conditions of the relative pose and then retain the stationary point with minimum cost function value as the global optimum solution. As an extension of [27], Li et al. [31] proposed a 2D robot relative pose estimation approach based on convex optimization. An MLE estimator is developed to improve the localization accuracy and handle the odometry uncertainties. The algorithm in [31] is sub-optimal because the range measurement noise at the initial timestamp is ignored. Trawny et al. [32] develop an algebraic robot relative localization method using 10 inter-robot range measurements. The algebraic methods relying on a small number of measurements are simple and efficient when the noise is low. However, the noise power of range measurement obtained by UWB modules exceeds the maximum noise power they can handle.

Inspired by RBL methods [19], [20], this study estimates robot relative pose using inter-robot ranges and odometry instead of a sensor network. Ego-motion is the movement of an observer, UWB module in our case. And odometry is an estimation of ego-motion. Previous studies either assume noiseless odometry [30] or ignore the accumulative property of robot position error [31]. This study builds a recursive model of accumulative position errors introduced by state transition vectors. Variance and bias are two important statistical indicators of an estimator. An asymptotically efficient estimator refers to an unbiased estimator with the variance overlapping with the Cramér–Rao lower bound (CRLB) [33]. Previous studies on robot relative localization [7], [26] lack theoretical analysis of estimators' variance and bias, which leaves the statistical behavior of the estimators unknown. This study proposes an asymptotically efficient estimator with theoretical validation. To summarize, the contribution of this study is threefold: (i) The CRLB of the robot relative pose is derived. (ii) A novel formulation for determining the robots' relative pose is presented. The odometry uncertainty is modeled by incorporating the state transition error and integrated with the measurement noise in a weighting matrix. (iii) An asymptotically efficient weighted semidefinite relaxation (WSDR) estimator is derived and theoretically validated. To the best of the author's knowledge, WSDR is the first theoretically validated asymptotically efficient estimator for robot relative localization.

We shall follow the convention of using bold lowercase and uppercase letters to denote column vectors and matrices, respectively. The notation $\star(i,:)$ and $\star(:,j)$ indicate the ith row and jth column of $\star$. Subvector $\star(i:j)$ contains the ith to the jth elements of $\star$. The notation $\star^o$ is the true value of $\star$ if it contains noise. $\mathbf{1}$ and $\mathbf{I}$ are the unity vector and the identity matrix. $\mathbf{0}$ and $\mathbf{O}$ are the vector and matrix with all zeros. $\mathrm{vec}(\star)$ is a column vector by stacking the columns of $\star$ together. $\mathrm{tr}(\star)$ calculates the trace of matrix $\star$. $\mathrm{blkdiag}(\star,*)$ is the block diagonal matrix with the diagonal block $\star$ and $*$. $\mathrm{angle}(\star)$ compute the phase angle in the interval $[-\pi,\pi]$ for $\star$. The symbol $\otimes$ represents the Kronecker product. $\mathbf{R}_\star = \left[\begin{smallmatrix}\cos\star & -\sin\star\\ \sin\star & \cos\star\end{smallmatrix}\right]$ is the 2D rotation matrix of $\star$. $\mathbf{R}'_\star = \left[\begin{smallmatrix}-\sin\star & -\cos\star\\ \cos\star & -\sin\star\end{smallmatrix}\right]$ is the derivative of $\mathbf{R}_\star$. $\boldsymbol{\nabla}_{\star *}$ is the derivative of $\star$ with respect to $*$.

II. Localization Scenario

This study considers a system consisting of two robots capable of measuring their ego-motion. Each robot has a UWB module that measures the range between the robots while

moving. Without loss of generality, we choose Robot 1 as the reference robot. Relative localization determines the relative orientation and position of Robot 2 in the body frame of Robot 1 at the initial moment.

Fig. 1 shows the relative localization scenario. The gray triangles and the white triangles represent the trajectories of Robot 1 and Robot 2, respectively. Our goal is to estimate the position of Robot 2 in the initial body frame of Robot 1. The state transition vectors representing the pose transformations between two consecutive moments are measured using IMUs and wheel encoders. A single UWB module is equipped on each robot. In Fig. 1, the UWB modules are mounted at the midpoint of the bottom edge of the triangles. By measuring the range between the UWB modules on the robots and the state transition vectors, we can estimate the initial relative pose. In total, we have M state transition vectors from the odometers and $M+1$ range measurements from the UWB modules. $\mathcal{A}_i$ and $\mathcal{B}_i$ are the body frames of Robot 1 and Robot 2 at timestamp i. The pose of Robot 2 in frame $\mathcal{A}_i$ is

$$\mathbf{u}_i = [\theta_i^T, \mathbf{p}_i^T]^T. \tag{1}$$

θ_i and $\mathbf{p}_i$ are the relative orientation and position of Robot 2 seen from the viewpoint of Robot 1 at the timestamp i. We aim to obtain the relative pose $\mathbf{u}_0$ at the initial timestamp 0. The subsequent relative pose $\mathbf{u}_i$, for $i = 1, \dots, M$, are calculated using the state transition model.

At timestamp i, we denote the pose of Robot 1 and Robot 2 in $\mathcal{A}_0$ and $\mathcal{B}_0$ as $\boldsymbol{v}_i^o = [\alpha_i^o, \mathbf{a}_i^{oT}]^T$ and $\boldsymbol{\omega}_i^o = [\beta_i^o, \mathbf{b}_i^{oT}]^T$. α_i^o and β_i^o represent the orientations of Robot 1 and Robot 2 in $\mathcal{A}_0$ and $\mathcal{B}_0$. $\mathbf{a}_i^o$ and $\mathbf{b}_i^o$ are the robot positions in $\mathcal{A}_0$ and $\mathcal{B}_0$. The i-th state transition vectors are denoted by $\dot{\boldsymbol{v}}_i^o = [\dot{\alpha}_i^o, \dot{\mathbf{a}}_i^{oT}]^T$ and $\dot{\boldsymbol{\omega}}_i^o = [\dot{\beta}_i^o, \dot{\mathbf{b}}_i^{oT}]^T$. The true poses of Robot 1 and Robot 2 at timestamp i are calculated in a recursive manner by

$$\boldsymbol{v}_i^o = \boldsymbol{v}_{i-1}^o + \mathbf{D}_{\boldsymbol{v}_{i-1}}^o \dot{\boldsymbol{v}}_i^o, \tag{2a}$$
$$\boldsymbol{\omega}_i^o = \boldsymbol{\omega}_{i-1}^o + \mathbf{D}_{\boldsymbol{\omega}_{i-1}}^o \dot{\boldsymbol{\omega}}_i^o, \tag{2b}$$

where

$$\mathbf{D}_{\boldsymbol{v}_{i-1}}^o = \mathrm{blkdiag}(1, \mathbf{R}_{\alpha_{i-1}^o}), \tag{3a}$$
$$\mathbf{D}_{\boldsymbol{\omega}_{i-1}}^o = \mathrm{blkdiag}(1, \mathbf{R}_{\beta_{i-1}^o}). \tag{3b}$$

At timestamp i, the pose of Robot 1 in $\mathcal{A}_{i-1}$ equals to the state transition vector $\dot{\boldsymbol{v}}_i^o$. The orientation and position of Robot 2 in $\mathcal{A}_{i-1}$ are

$$\theta_{\mathcal{A}_{i-1},i} = \theta_{i-1} + \dot{\beta}_i^o, \tag{4a}$$
$$\mathbf{p}_{\mathcal{A}_{i-1},i} = \mathbf{R}_{\theta_{i-1}} \dot{\mathbf{b}}_i^o + \mathbf{p}_{i-1}. \tag{4b}$$

The relative pose of Robot 2 in Robot 1's frame can be updated using the previous relative pose and the state transition vectors,

$$\theta_i = -\dot{\alpha}_i^o + \theta_{i-1} + \dot{\beta}_i^o, \tag{5a}$$
$$\mathbf{p}_i = \mathbf{R}_{\dot{\alpha}_i^o}^T \mathbf{R}_{\theta_{i-1}} \dot{\mathbf{b}}_i^o + \mathbf{R}_{\dot{\alpha}_i^o}^T \mathbf{p}_{i-1} - \mathbf{R}_{\dot{\alpha}_i^o}^T \dot{\mathbf{a}}_i^o \tag{5b}$$

With an estimate of the initial relative pose, the state transition model (5a) and (5b) can be applied to calculate the robot's relative pose at any moment. However, the relative pose error accumulates over time because of the noisy odometry information. Filtering-based methods are applied to incorporate the subsequent range measurements and reduce the accumulative relative pose error.

UWB modules are placed at $\mathbf{s}_0$ and $\mathbf{t}_0$ in the body frame of Robot 1 and Robot 2. The positions of UWB modules mounted on Robot 1 and Robot 2 at timestamp i in their initial body frame $\mathcal{A}_0$ and $\mathcal{B}_0$ are given by

$$\mathbf{s}_i^o = \mathbf{R}_{\alpha_i^o} \mathbf{s}_0 + \mathbf{a}_i^o, \tag{6a}$$
$$\mathbf{t}_i^o = \mathbf{R}_{\beta_i^o} \mathbf{t}_0 + \mathbf{b}_i^o, \tag{6b}$$

respectively. The true range between the two UWB modules at timestamp i is

$$d_i^o = \|\mathbf{R}_{\theta_0} \mathbf{t}_i^o + \mathbf{p}_0 - \mathbf{s}_i^o\|. \tag{7}$$

The inter-robot range vector of all timestamps is $\mathbf{d}^o = [d_0^o, \dots, d_M^o]^T$. In practice, the range measurements $\mathbf{d}$ contains the additive measurement noise $\mathbf{n}_\mathbf{d} = [n_0, \dots, n_M]^T$, which follows Gaussian distribution $\mathcal{N}(\mathbf{0}, \mathbf{Q}_\mathbf{d})$ [18].

In addition to the UWB measurements noise, the state transition vector $\dot{\boldsymbol{v}}_i$ and $\dot{\boldsymbol{\omega}}_i$ contain noise, which are denoted as $\Delta\dot{\boldsymbol{v}}_i$ and $\Delta\dot{\boldsymbol{\omega}}_i$, respectively. We assume the state transition errors between any two timestamps are independent and identically distributed (IID). $\Delta\dot{\boldsymbol{v}}_i$ and $\Delta\dot{\boldsymbol{\omega}}_i$ follow Gaussian distribution $\mathcal{N}(\mathbf{0}, \mathbf{Q}_{\dot{\boldsymbol{v}}})$ and $\mathcal{N}(\mathbf{0}, \mathbf{Q}_{\dot{\boldsymbol{\omega}}})$ [34]. UWB module position $\mathbf{s}_i$ and $\mathbf{t}_i$ contain accumulative odometry error $\Delta\mathbf{s}_i$ and $\Delta\mathbf{t}_i$. Stacking $\mathbf{s}_i$ and $\mathbf{t}_i$ in vector form gives $\mathbf{s}$ and $\mathbf{t}$. Applying the first-order Taylor expansion, the covariance matrices of $\mathbf{s}$ and $\mathbf{t}$ are

$$\mathbf{Q}_\mathbf{s} = \boldsymbol{\nabla}_{\mathbf{s}^o \boldsymbol{v}^o} \boldsymbol{\nabla}_{\boldsymbol{v}^o \Delta\dot{\boldsymbol{v}}} (\mathbf{I} \otimes \mathbf{Q}_{\dot{\boldsymbol{v}}}) \boldsymbol{\nabla}_{\boldsymbol{v}^o \Delta\dot{\boldsymbol{v}}}^T \boldsymbol{\nabla}_{\mathbf{s}^o \boldsymbol{v}^o}^T, \tag{8a}$$
$$\mathbf{Q}_\mathbf{t} = \boldsymbol{\nabla}_{\mathbf{t}^o \boldsymbol{\omega}^o} \boldsymbol{\nabla}_{\boldsymbol{\omega}^o \Delta\dot{\boldsymbol{\omega}}} (\mathbf{I} \otimes \mathbf{Q}_{\dot{\boldsymbol{\omega}}}) \boldsymbol{\nabla}_{\boldsymbol{\omega}^o \Delta\dot{\boldsymbol{\omega}}}^T \boldsymbol{\nabla}_{\mathbf{t}^o \boldsymbol{\omega}^o}^T. \tag{8b}$$

The robot pose error is introduced by the state transition error and the robot pose error from the previous moment. Replacing the true robot poses and the true state transition vectors in (2a) with the noisy version and neglecting the higher order error terms yield

$$\boldsymbol{v}_i = \boldsymbol{v}_{i-1}^o + \mathbf{D}_{\boldsymbol{v}_{i-1}}^o \dot{\boldsymbol{v}}_i^o + \boldsymbol{\nabla}_{\boldsymbol{v}_i^o \boldsymbol{v}_{i-1}^o} \Delta\boldsymbol{v}_{i-1} + \mathbf{D}_{\boldsymbol{v}_{i-1}}^o \Delta\dot{\boldsymbol{v}}_i, \tag{9}$$

where $\boldsymbol{\nabla}_{\boldsymbol{v}_i^o \boldsymbol{v}_{i-1}^o} = \begin{bmatrix} 1 & \mathbf{0}^T \\ \mathbf{R}'_{\alpha_{i-1}^o} \dot{\mathbf{a}}_i^o & \mathbf{I} \end{bmatrix}$. $\Delta\boldsymbol{v}_{i-1}$ is the odometry error of the previous step. Substituting $\dot{\boldsymbol{v}}_i^o = \dot{\boldsymbol{v}}_i - \Delta\dot{\boldsymbol{v}}_i$ into (2a) and taking derivative of $\boldsymbol{v}_i^o$ with respect to $\Delta\dot{\boldsymbol{v}}_i$ yield $\boldsymbol{\nabla}_{\boldsymbol{v}_i^o \Delta\dot{\boldsymbol{v}}_i} = -\mathbf{D}_{\boldsymbol{v}_i}^o$. The Jacobian matrix of $\boldsymbol{v}^o$ with respect to $\Delta\dot{\boldsymbol{v}}$ is

$$\boldsymbol{\nabla}_{\boldsymbol{v}^o \Delta\dot{\boldsymbol{v}}} = -\begin{bmatrix} \mathbf{D}_{\boldsymbol{v}_0}^o & \dots & \mathbf{0} \\ \vdots & \ddots & \vdots \\ \boldsymbol{\nabla}_{\boldsymbol{v}_M^o, \boldsymbol{v}_{M-1}^o} \dots \boldsymbol{\nabla}_{\boldsymbol{v}_2^o, \boldsymbol{v}_1^o} \mathbf{D}_{\boldsymbol{v}_0}^o & \dots & \mathbf{D}_{\boldsymbol{v}_{M-1}}^o \end{bmatrix}. \tag{10}$$

According to (6a), the UWB module position only depends on the current robot pose. Taking the derivative of UWB module positions with respect to the current robot pose gives

$$\boldsymbol{\nabla}_{\mathbf{s}^o \boldsymbol{v}^o} = \mathrm{blkdiag}(\boldsymbol{\nabla}_{\mathbf{s}_1^o \boldsymbol{v}_1^o}, \dots, \boldsymbol{\nabla}_{\mathbf{s}_M^o \boldsymbol{v}_M^o}), \tag{11}$$

where $\boldsymbol{\nabla}_{\mathbf{s}_i^o \boldsymbol{v}_i^o} = [\mathbf{R}'_{\alpha_i^o} \mathbf{s}_0, \mathbf{I}]$.

$\boldsymbol{\nabla}_{\boldsymbol{\omega}^o \Delta\dot{\boldsymbol{\omega}}}$ and $\boldsymbol{\nabla}_{\mathbf{t}^o \boldsymbol{\omega}^o}$ can be computed following the similar steps in (9)-(11). The derivation of $\mathbf{Q}_\mathbf{t}$ in (8b) is omitted.

III. Robot Relative Pose Estimation

A. Problem Formulation

This section derives a formulation and a WSDR solver for robot relative pose estimation in the presence of robot position error and measurement noise. Two moving robots replace the sensor network in the RBL problem. The UWB modules mounted on the robots obtain a single range measurement at each timestamp.

We start with the noise-free inter-robot range and UWB position. Squaring both sides of (7) gives

$$\begin{aligned} d_i^{o2} - \mathbf{t}_i^{oT}\mathbf{t}_i^o - \mathbf{s}_i^{oT}\mathbf{s}_i^o + 2\mathbf{s}_i^{oT}\mathbf{R}_{\theta_0}\mathbf{t}_i^o + 2\mathbf{s}_i^{oT}\mathbf{p}_0 \\ - 2\mathbf{t}_i^{oT}\mathbf{R}_{\theta_0}^T\mathbf{p}_0 - \mathbf{p}_0^T\mathbf{p}_0 = \boldsymbol{\eta}_i. \end{aligned} \tag{12}$$

$\boldsymbol{\eta}_i$ is the residual, which is equal to zero in the noise-free case. When UWB measurement noise and odometry error exist, we replace $\mathbf{s}_i^o$ with $\mathbf{s}_i$, $\mathbf{t}_i^o$ with $\mathbf{t}_i$, and d_i^o with d_i. Denote $\boldsymbol{\Gamma} = \left[\begin{smallmatrix} 0 & 1 & -1 & 0 \\ 1 & 0 & 0 & 1 \end{smallmatrix}\right]^T$ and $\mathbf{y}_0 = [\sin\theta_0, \cos\theta_0]^T$, the vectorized rotation matrix is $\mathrm{vec}(\mathbf{R}_{\theta_0}) = \boldsymbol{\Gamma}\mathbf{y}_0$. Applying the "vec-trick" of the Kronecker product to (12), we have

$$\begin{aligned} d_i^2 - \mathbf{t}_i^T\mathbf{t}_i - \mathbf{s}_i^T\mathbf{s}_i + 2(\mathbf{t}_i^T \otimes \mathbf{s}_i^T)\boldsymbol{\Gamma}\mathbf{y}_0 \\ + 2\mathbf{s}_i^T\mathbf{p}_0 - 2\mathbf{t}_i^T\mathbf{R}_{\theta_0}^T\mathbf{p}_0 - \mathbf{p}_0^T\mathbf{p}_0 = \boldsymbol{\eta}_i. \end{aligned} \tag{13}$$

The residual is given by

$$\begin{aligned} \boldsymbol{\eta}_i \approx 2d_i^o n_i + (-2\mathbf{s}_i^{oT} + 2\mathbf{t}_i^{oT}\mathbf{R}_{\theta_0}^T + 2\mathbf{p}_0^T)\Delta\mathbf{s}_i \\ + (-2\mathbf{t}_i^{oT} + 2\mathbf{s}_i^{oT}\mathbf{R}_{\theta_0} - 2\mathbf{p}_0^T\mathbf{R}_{\theta_0})\Delta\mathbf{t}_i, \end{aligned} \tag{14}$$

where the higher-order noise terms are ignored. Stacking (13) into the matrix form and defining the augmented unknown parameter vector as $\mathbf{v} = [\mathbf{y}_0^T, \mathbf{p}_0^T, \mathbf{p}_0^T\mathbf{R}_{\theta_0}, \mathbf{p}_0^T\mathbf{p}_0]^T$ give

$$\mathbf{h} - \mathbf{G}\mathbf{v} = \mathbf{B}_\mathbf{d}\mathbf{n}_\mathbf{d} + \mathbf{B}_\mathbf{s}\Delta\mathbf{s} + \mathbf{B}_\mathbf{t}\Delta\mathbf{t}, \tag{15}$$

where

$$\mathbf{G}(i+1,:) = \begin{bmatrix} -2(\mathbf{t}_i^T \otimes \mathbf{s}_i^T)\boldsymbol{\Gamma} & -2\mathbf{s}_i^T & 2\mathbf{t}_i^T & 1 \end{bmatrix}, \tag{16}$$

$$\mathbf{h}(i+1,1) = d_i^2 - \mathbf{t}_i^T\mathbf{t}_i - \mathbf{s}_i^T\mathbf{s}_i. \tag{17}$$

$\mathbf{B}_\mathbf{d}$ is a diagonal matrix with diagonal element $\mathbf{B}_\mathbf{d}(i+1, i+1) = 2d_i^o$. The UWB position error $\Delta\mathbf{s}$ and $\Delta\mathbf{t}$ affect the residual through the coefficient matrix

$$\mathbf{B}_\mathbf{s} = \mathrm{blkdiag}(\mathbf{0}, \boldsymbol{\zeta}_{\mathbf{s}_1}, \ldots, \boldsymbol{\zeta}_{\mathbf{s}_M}), \tag{18a}$$

$$\mathbf{B}_\mathbf{t} = \mathrm{blkdiag}(\mathbf{0}, \boldsymbol{\zeta}_{\mathbf{t}_1}, \ldots, \boldsymbol{\zeta}_{\mathbf{t}_M}). \tag{18b}$$

From (14), we have $\boldsymbol{\zeta}_{\mathbf{s}_i} = -2\mathbf{s}_i^{oT} + 2\mathbf{t}_i^{oT}\mathbf{R}_{\theta_0}^T + 2\mathbf{p}_0^T$ and $\boldsymbol{\zeta}_{\mathbf{t}_i} = -2\mathbf{t}_i^{oT} + 2\mathbf{s}_i^{oT}\mathbf{R}_{\theta_0} - 2\mathbf{p}_0^T\mathbf{R}_{\theta_0}$. In practice, we replace the noiseless variables d_i^o, $\mathbf{s}_i^o$, and $\mathbf{t}_i^o$ with measurements from UWB modules and odometers in $\mathbf{B}_\mathbf{d}$, $\mathbf{B}_\mathbf{s}$, and $\mathbf{B}_\mathbf{t}$ since the higher order noise terms can be neglected. Note that $\mathbf{B}_\mathbf{s}$ and $\mathbf{B}_\mathbf{t}$ contain unknown $\mathbf{R}_{\theta_0}$ and $\mathbf{p}_0$. We first compute $\mathbf{v}$ with an identity weighting matrix and then substitute the first four elements back to construct $\mathbf{B}_\mathbf{s}$ and $\mathbf{B}_\mathbf{t}$.

B. Weighted Semidefinite Relaxation

This subsection constructs a quadratically constrained quadratic programming (QCQP) problem from the formulation in Section III-A and solves the QCQP problem using the semidefinite relaxation (SDR) technique. The length of $\mathbf{v}$ is equal to seven, and the degree of freedom is equal to three. We introduce four constraints and reformulate the relative localization problem in (15) as

$$\min_{\mathbf{v}} \quad (\mathbf{G}\mathbf{v} - \mathbf{h})^T\mathbf{W}(\mathbf{G}\mathbf{v} - \mathbf{h}) \tag{19a}$$

$$\text{s.t.} \quad \mathbf{v}(1)^2 + \mathbf{v}(2)^2 = 1 \tag{19b}$$

$$\mathbf{v}(1)\mathbf{v}(4) + \mathbf{v}(2)\mathbf{v}(3) = \mathbf{v}(5) \tag{19c}$$

$$\mathbf{v}(2)\mathbf{v}(4) - \mathbf{v}(1)\mathbf{v}(3) = \mathbf{v}(6) \tag{19d}$$

$$\mathbf{v}(3)^2 + \mathbf{v}(4)^2 = \mathbf{v}(7) \tag{19e}$$

The weighting matrix is given by

$$\mathbf{W} = (\mathbf{B}_\mathbf{d}\mathbf{Q}_\mathbf{d}\mathbf{B}_\mathbf{d} + \mathbf{B}_\mathbf{s}\mathbf{Q}_\mathbf{s}\mathbf{B}_\mathbf{s}^T + \mathbf{B}_\mathbf{t}\mathbf{Q}_\mathbf{t}\mathbf{B}_\mathbf{t}^T)^{-1}. \tag{20}$$

We denote $\mathbf{V} = \mathbf{v}\mathbf{v}^T$ and allow the rank of $\mathbf{V}$ to be larger than 1. (19) is rewritten as

$$\min_{\mathbf{V},\mathbf{v}} \quad \mathbf{G}^T\mathbf{W}\mathbf{G}\mathbf{V} - \mathbf{h}^T\mathbf{W}\mathbf{G}\mathbf{v} \tag{21a}$$

$$\text{s.t.} \quad \begin{bmatrix} 1 & \mathbf{v}^T \\ \mathbf{v} & \mathbf{V} \end{bmatrix} \succeq 0 \tag{21b}$$

$$1 - \mathrm{tr}(\mathbf{M}_1\mathbf{V}) = 0 \tag{21c}$$

$$\mathbf{v}(5) - \mathrm{tr}(\mathbf{M}_2\mathbf{V}) = 0 \tag{21d}$$

$$\mathbf{v}(6) - \mathrm{tr}(\mathbf{M}_3\mathbf{V}) = 0 \tag{21e}$$

$$\mathbf{v}(7) - \mathrm{tr}(\mathbf{M}_4\mathbf{V}) = 0 \tag{21f}$$

The constant term $\mathbf{h}^T\mathbf{W}\mathbf{h}$ in (19a) is removed because it does not affect the value of $\mathbf{v}$. $\mathbf{M}_k$ for $k = 1, \ldots, 4$ are 7×7 sparse matrices with nonzero elements specified as follows:

$$\mathbf{M}_1(1,1) = \mathbf{M}_1(2,2) = 1, \tag{22a}$$

$$\mathbf{M}_2(1,4) = \mathbf{M}_2(4,1) = \mathbf{M}_2(2,3) = \mathbf{M}_2(3,2) = 0.5, \tag{22b}$$

$$\mathbf{M}_3(1,3) = \mathbf{M}_3(3,1) = -0.5,\ \mathbf{M}_3(2,4) = \mathbf{M}_3(4,2) = 0.5, \tag{22c}$$

$$\mathbf{M}_4(3,3) = \mathbf{M}_4(4,4) = 1. \tag{22d}$$

Optimizing the constrained cost function (21) using the CVX toolbox in Matlab [36] gives $\hat{\mathbf{V}}$ and $\hat{\mathbf{v}}$. We discard $\hat{\mathbf{V}}$ and compute the relative pose using $\hat{\mathbf{v}}$. The WSDR solution is

$$\hat{\mathbf{u}}_0 = \begin{bmatrix} \mathrm{angle}(\hat{\mathbf{v}}(2) + \sqrt{-1}\hat{\mathbf{v}}(1)) \\ \hat{\mathbf{v}}(3:4) \end{bmatrix}. \tag{23}$$

We list the steps of WSDR in Algorithm 1 and summarize workflow of relative robot localization in Fig. 2. WSDR utilizes range measurements and state transition vectors from multiple timestamps. And it combines range measurement noise and state transition errors using a weighting matrix.

In many circumstances, we are interested in the pose of the most recent moment instead of the initial pose. Fortunately, the initial pose estimation methods can be adapted to determine the current pose between two robots after some simple modifications in Appendix A.

IV. Performance Analysis

A. Cramér–Rao Lower Bound

The CRLB is a lower bound on the variance of an unbiased estimator for a deterministic parameter, indicating the minimum achievable variance. In this section, we would like to derive the

Algorithm 1: WSDR

Data: range measurement vector $\mathbf{d}$, state transition vector $\boldsymbol{\upsilon}_i$ and $\boldsymbol{\omega}_i$, for $i = 1, \ldots, M$

Result: initial robot relative pose $\mathbf{u}_0$

Compute $\mathbf{Q_s}$ and $\mathbf{Q_t}$ using (8);
Compute $\mathbf{G}$ and $\mathbf{h}$ using (16) and (17);
Compute $\mathbf{M}_i$ for $i = 1, \ldots, 4$ using (22);
Initialize $\mathbf{W} = \mathbf{I}$;
Solve $\mathbf{v}$ by optimizing (21);
Substitute $\mathbf{v}$ into (18) to compute $\mathbf{B_s}$ and $\mathbf{B_t}$;
Update $\mathbf{W}$ using (20);
Solve $\hat{\mathbf{v}}$ by optimizing (21) with updated $\mathbf{W}$;
Compute $\mathbf{u}_0$ using (23)

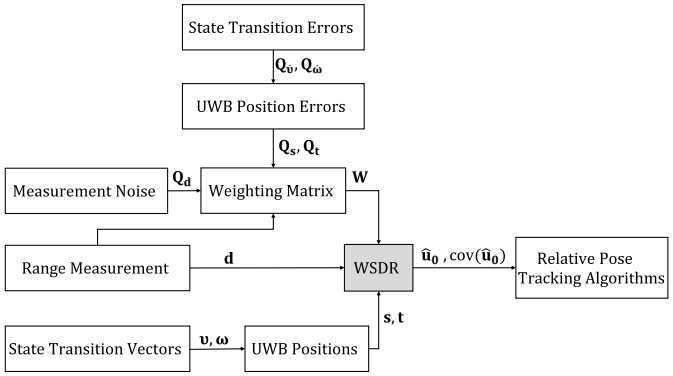

Fig. 2. Flowchart of robot relative localization.

CRLB of the initial relative pose $\mathbf{u}_0$ when the measurement noise and the robot pose transition error exist. We start the derivation with the logarithm of the joint probability density function.

$$\begin{aligned}\ln p = k &- \frac{1}{2}(\mathbf{d}-\mathbf{d}^o)^T\mathbf{Q_d}^{-1}(\mathbf{d}-\mathbf{d}^o) \\ &- \frac{1}{2}\Delta\dot{\boldsymbol{\upsilon}}^T(\mathbf{I}\otimes\mathbf{Q}_{\dot{\boldsymbol{\upsilon}}})^{-1}\Delta\dot{\boldsymbol{\upsilon}} - \frac{1}{2}\Delta\dot{\boldsymbol{\omega}}^T(\mathbf{I}\otimes\mathbf{Q}_{\dot{\boldsymbol{\omega}}})^{-1}\Delta\dot{\boldsymbol{\omega}}.\end{aligned} \tag{24}$$

Denote $\Delta\dot{\boldsymbol{\varphi}} = [\Delta\dot{\boldsymbol{\upsilon}}^T, \Delta\dot{\boldsymbol{\omega}}^T]^T$ and $\bar{\mathbf{Q}}_{\dot{\boldsymbol{\varphi}}} = \text{blkdiag}(\mathbf{I}\otimes\mathbf{Q}_{\dot{\boldsymbol{\upsilon}}}, \mathbf{I}\otimes\mathbf{Q}_{\dot{\boldsymbol{\omega}}})$. The Fisher information matrix (FIM) of the unknown parameter vector $\boldsymbol{\gamma} = [\mathbf{u}_0^T, \Delta\dot{\boldsymbol{\varphi}}^T]^T$ is

$$\text{FIM}(\boldsymbol{\gamma}) = \begin{bmatrix} \boldsymbol{\nabla}_{\mathbf{d}^o\mathbf{u}_0}^T\mathbf{Q_d}^{-1}\boldsymbol{\nabla}_{\mathbf{d}^o\mathbf{u}_0} & \boldsymbol{\nabla}_{\mathbf{d}^o\mathbf{u}_0}^T\mathbf{Q_d}^{-1}\boldsymbol{\nabla}_{\mathbf{d}^o\Delta\dot{\boldsymbol{\varphi}}} \\ \boldsymbol{\nabla}_{\mathbf{d}^o\Delta\dot{\boldsymbol{\varphi}}}^T\mathbf{Q_d}^{-1}\boldsymbol{\nabla}_{\mathbf{d}^o\mathbf{u}_0} & \boldsymbol{\nabla}_{\mathbf{d}^o\Delta\dot{\boldsymbol{\varphi}}}^T\mathbf{Q_d}^{-1}\boldsymbol{\nabla}_{\mathbf{d}^o\Delta\dot{\boldsymbol{\varphi}}} + \bar{\mathbf{Q}}_{\dot{\boldsymbol{\varphi}}}^{-1} \end{bmatrix}, \tag{25}$$

Taking the derivative of $\mathbf{d}^o$ with respect to $\mathbf{u}_0$ give $\boldsymbol{\nabla}_{\mathbf{d}^o\mathbf{u}_0} = [\boldsymbol{\nabla}_{d_0^o\mathbf{u}_0}^T, \ldots, \boldsymbol{\nabla}_{d_M^o\mathbf{u}_0}^T]^T$, where

$$\boldsymbol{\nabla}_{d_i^o\mathbf{u}_0} = \boldsymbol{\rho}_i^{oT}\begin{bmatrix}\mathbf{R}'_{\theta_0}\mathbf{t}_i^o & \mathbf{I}\end{bmatrix}, \tag{26a}$$

$$\boldsymbol{\rho}_i^o = \frac{\mathbf{R}_{\theta_0}\mathbf{t}_i^o + \mathbf{p}_0 - \mathbf{s}_i^o}{\|\mathbf{R}_{\theta_0}\mathbf{t}_i^o + \mathbf{p}_0 - \mathbf{s}_i^o\|}. \tag{26b}$$

The first-order derivative of $\mathbf{d}$ with respect to the odometry uncertainties is $\boldsymbol{\nabla}_{\mathbf{d}^o\Delta\dot{\boldsymbol{\varphi}}} = [\boldsymbol{\nabla}_{\mathbf{d}^o\Delta\dot{\boldsymbol{\upsilon}}}, \boldsymbol{\nabla}_{\mathbf{d}^o\Delta\dot{\boldsymbol{\omega}}}]$. The lower triangular matrix $\boldsymbol{\nabla}_{\mathbf{d}^o\Delta\dot{\boldsymbol{\upsilon}}}$ is given by

$$\boldsymbol{\nabla}_{\mathbf{d}^o\Delta\dot{\boldsymbol{\upsilon}}} = \begin{bmatrix} \mathbf{0}^T & \cdots & \mathbf{0}^T \\ \boldsymbol{\nabla}_{d_1^o\Delta\dot{\boldsymbol{\upsilon}}_1} & \ddots & \vdots \\ \vdots & \ddots & \mathbf{0}^T \\ \boldsymbol{\nabla}_{d_M^o\Delta\dot{\boldsymbol{\upsilon}}_1} & \cdots & \boldsymbol{\nabla}_{d_M^o\Delta\dot{\boldsymbol{\upsilon}}_M} \end{bmatrix}. \tag{27}$$

$\boldsymbol{\nabla}_{d_i^o\Delta\dot{\boldsymbol{\upsilon}}_j}$ is calculated recursively by

$$\boldsymbol{\nabla}_{d_i^o\Delta\dot{\boldsymbol{\upsilon}}_j} = -\boldsymbol{\nabla}_{d_i^o\boldsymbol{\upsilon}_i^o}\boldsymbol{\nabla}_{\boldsymbol{\upsilon}_i^o\boldsymbol{\upsilon}_{i-1}^o}\ldots\boldsymbol{\nabla}_{\boldsymbol{\upsilon}_j^o\boldsymbol{\upsilon}_{j-1}^o}\mathbf{D}_{\boldsymbol{\upsilon}_{j-1}}^o, \quad i \geq j, \tag{28}$$

where $\boldsymbol{\nabla}_{d_i^o\boldsymbol{\upsilon}_i^o} = -\boldsymbol{\rho}_i^{oT}[\mathbf{R}'_{\alpha_i^o}\mathbf{s}_0, \mathbf{I}]$. $\mathbf{D}_{\boldsymbol{\upsilon}_{i-1}}^o$ is given by (3a), and $\boldsymbol{\nabla}_{\boldsymbol{\upsilon}_i^o\boldsymbol{\upsilon}_{i-1}^o}$ is defined below equation (9), respectively.

Note that $\boldsymbol{\nabla}_{d_i^o\boldsymbol{\omega}_i^o} = \boldsymbol{\rho}_i^{oT}[\mathbf{R}_{\theta_0}\mathbf{R}'_{\beta_i^o}\mathbf{t}_0, \ \mathbf{R}_{\theta_0}]$. $\boldsymbol{\nabla}_{\mathbf{d}^o\Delta\dot{\boldsymbol{\omega}}}$ is computed following the similar steps as $\boldsymbol{\nabla}_{\mathbf{d}^o\Delta\dot{\boldsymbol{\upsilon}}}$.

The CRLB of the relative pose is equal to the top-left 3×3 block of the inverse FIM. Applying the block matrix inversion formula, we have

$$\begin{aligned}\text{CRLB}(\mathbf{u}_0)^{-1} &= \boldsymbol{\nabla}_{\mathbf{d}^o\mathbf{u}_0}^T\mathbf{Q_d}^{-1}\boldsymbol{\nabla}_{\mathbf{d}^o\mathbf{u}_0} - \boldsymbol{\nabla}_{\mathbf{d}^o\mathbf{u}_0}^T\mathbf{Q_d}^{-1}\boldsymbol{\nabla}_{\mathbf{d}^o\Delta\dot{\boldsymbol{\varphi}}} \\ &\times(\boldsymbol{\nabla}_{\mathbf{d}^o\Delta\dot{\boldsymbol{\varphi}}}^T\mathbf{Q_d}^{-1}\boldsymbol{\nabla}_{\mathbf{d}^o\Delta\dot{\boldsymbol{\varphi}}} + \bar{\mathbf{Q}}_{\dot{\boldsymbol{\varphi}}}^{-1})^{-1}\boldsymbol{\nabla}_{\mathbf{d}^o\Delta\dot{\boldsymbol{\varphi}}}^T\mathbf{Q_d}^{-1}\boldsymbol{\nabla}_{\mathbf{d}^o\mathbf{u}_0}.\end{aligned} \tag{29}$$

B. Theoretical Covariance: WSDR

In this subsection, we will demonstrate $\hat{\mathbf{u}}_0$ in (23) achieves the CRLB performance in (29).

By defining $\mathbf{B} = [\mathbf{B_d}, \mathbf{B_s}, \mathbf{B_t}]^T$ and $\mathbf{n} = [\mathbf{n_d}^T, \Delta\mathbf{s}^T, \Delta\mathbf{t}^T]^T$, and replacing $\mathbf{v}$ with $\mathbf{v}^o + \Delta\hat{\mathbf{v}}$, (19) becomes

$$\min_{\Delta\hat{\mathbf{v}}} \quad (\mathbf{G}\Delta\hat{\mathbf{v}} + \mathbf{B}\mathbf{n})^T\mathbf{W}(\mathbf{G}\Delta\hat{\mathbf{v}} + \mathbf{B}\mathbf{n}) \tag{30a}$$

$$\text{s.t.} \quad \mathbf{K}^T\Delta\hat{\mathbf{v}} = \mathbf{0}, \tag{30b}$$

where

$$\begin{aligned}\mathbf{K} &= \boldsymbol{\nabla}_{\mathbf{f}^o\mathbf{v}^o}^T, \\ &= \left[\begin{array}{cccc|c} 2\sin\theta_0 & 2\cos\theta_0 & 0 & 0 & \mathbf{0} \\ \mathbf{p}_0(2) & \mathbf{p}_0(1) & \cos\theta_0 & \sin\theta_0 & \\ -\mathbf{p}_0(1) & \mathbf{p}_0(2) & -\sin\theta_0 & \cos\theta_0 & -\mathbf{I} \\ 0 & 0 & 2\mathbf{p}_0(1) & 2\mathbf{p}_0(2) & \end{array}\right]^T.\end{aligned} \tag{31}$$

From (30b), $\boldsymbol{\Delta}\hat{\mathbf{v}}$ lies in the null space of $\mathbf{K}$. We have

$$\boldsymbol{\Delta}\hat{\mathbf{v}} = \mathbf{M}\mathbf{q}, \tag{32}$$

where $\mathbf{M}$ is a matrix whose columns form an orthogonal basis of the null space of $\mathbf{K}$, and $\mathbf{q}$ is a vector of independent variables. From (23), we have

$$\boldsymbol{\nabla}_{\mathbf{v}\mathbf{u}_0} = \begin{bmatrix} \cos\theta_0 & -\sin\theta_0 & 0 & 0 & c_1 & c_2 & 0 \\ 0 & 0 & 1 & 0 & \cos\theta_0 & -\sin\theta_0 & 2\mathbf{p}_0(1) \\ 0 & 0 & 0 & 1 & \sin\theta_0 & \cos\theta_0 & 2\mathbf{p}_0(2) \end{bmatrix}^T \tag{33}$$

where $c_1 = -\mathbf{p}_0(1)\sin\theta_0 + \mathbf{p}_0(2)\cos\theta_0$ and $c_2 = -\mathbf{p}_0(1)\cos\theta_0 - \mathbf{p}_0(2)\sin\theta_0$. After some trivial mathematical manipulation, we prove $\mathbf{K}^T\boldsymbol{\nabla}_{\mathbf{v}\mathbf{u}_0} = \mathbf{O}$. The independent columns of $\boldsymbol{\nabla}_{\mathbf{v}\mathbf{u}_0}$ spans the null space of $\mathbf{K}$. Thus, we let $\mathbf{M} = \boldsymbol{\nabla}_{\mathbf{v}\mathbf{u}_0}$. The cost function (30a) becomes

$$(\mathbf{G}\mathbf{M}\mathbf{q} + \mathbf{B}\mathbf{n})^T\mathbf{W}(\mathbf{G}\mathbf{M}\mathbf{q} + \mathbf{B}\mathbf{n}). \tag{34}$$

The optimal solution of $\mathbf{q}$ is

$$\mathbf{q} = -(\mathbf{M}^T\mathbf{J}\mathbf{M})^{-1}\mathbf{M}^T\mathbf{G}^T\mathbf{W}\mathbf{B}\mathbf{n}, \tag{35}$$

where $\mathbf{J} = \mathbf{G}^T\mathbf{W}\mathbf{G}$. Taking expectation of $\boldsymbol{\Delta}\hat{\mathbf{v}}$ gives $\mathbb{E}[\boldsymbol{\Delta}\hat{\mathbf{v}}] = \mathbf{M}\mathbb{E}[\mathbf{q}] = \mathbf{0}$. WSDR is unbiased when higher-order noise terms are negligible. Multiplying both sides of (35) by their transpose and taking expectations gives

$$\mathbb{E}[\mathbf{q}\mathbf{q}^T] = (\mathbf{M}^T\mathbf{J}\mathbf{M})^{-1}. \tag{36}$$

And hence, $\mathrm{cov}(\hat{\mathbf{v}}) = \mathbf{M}(\mathbf{M}^T\mathbf{J}\mathbf{M})^{-1}\mathbf{M}^T$.

The theoretical covariance matrix for the unbiased estimator WSDR is

$$\mathrm{cov}(\hat{\mathbf{u}}_0) = \boldsymbol{\nabla}^{\dagger}_{\mathbf{v}\mathbf{u}_0}\mathrm{cov}(\hat{\mathbf{v}})(\boldsymbol{\nabla}^{\dagger}_{\mathbf{v}\mathbf{u}_0})^T = (\mathbf{M}^T\mathbf{J}\mathbf{M})^{-1}. \tag{37}$$

Substituting (8a) and (8b) into (20) yields

$$\mathbf{W} = (\mathbf{B}_{\mathbf{d}}\mathbf{Q}_{\mathbf{d}}\mathbf{B}_{\mathbf{d}} + \mathbf{B}_{\dot{\boldsymbol{\varphi}}}\bar{\mathbf{Q}}_{\dot{\boldsymbol{\varphi}}}\mathbf{B}^T_{\dot{\boldsymbol{\varphi}}})^{-1}, \tag{38}$$

$$\mathbf{B}_{\dot{\boldsymbol{\varphi}}} = \left[\mathbf{B}_{\mathbf{s}}\boldsymbol{\nabla}_{\mathbf{s}^o\boldsymbol{v}^o}\boldsymbol{\nabla}_{\boldsymbol{v}^o\Delta\dot{\boldsymbol{v}}}, \mathbf{B}_{\mathbf{t}}\boldsymbol{\nabla}_{\mathbf{t}^o\boldsymbol{\omega}^o}\boldsymbol{\nabla}_{\boldsymbol{\omega}^o\Delta\dot{\boldsymbol{\omega}}}\right]. \tag{39}$$

Applying Woodbury matrix identity to (38) gives

$$\begin{aligned}\mathbf{W} &= \mathbf{B}_{\mathbf{d}}^{-1}\mathbf{Q}_{\mathbf{d}}^{-1}\mathbf{B}_{\mathbf{d}}^{-1} + \mathbf{B}_{\mathbf{d}}^{-1}\mathbf{Q}_{\mathbf{d}}^{-1}\mathbf{B}_{\mathbf{d}}^{-1}\mathbf{B}_{\dot{\boldsymbol{\varphi}}} \\ &\times (\bar{\mathbf{Q}}_{\dot{\boldsymbol{\varphi}}}^{-1} + \mathbf{B}^T_{\dot{\boldsymbol{\varphi}}}\mathbf{B}_{\mathbf{d}}^{-1}\mathbf{Q}_{\mathbf{d}}^{-1}\mathbf{B}_{\mathbf{d}}^{-1}\mathbf{B}_{\dot{\boldsymbol{\varphi}}})^{-1}\mathbf{B}^T_{\dot{\boldsymbol{\varphi}}}\mathbf{B}_{\mathbf{d}}^{-1}\mathbf{Q}_{\mathbf{d}}^{-1}\mathbf{B}_{\mathbf{d}}^{-1}.\end{aligned} \tag{40}$$

Substituting (40) and the definition of $\mathbf{J}$ into (37) gives

$$\begin{aligned}\mathrm{cov}(\hat{\mathbf{u}}_0)^{-1} &= \mathbf{G}_3^T\mathbf{Q}_{\mathbf{d}}^{-1}\mathbf{G}_3 \\ &- \mathbf{G}_3^T\mathbf{Q}_{\mathbf{d}}^{-1}\mathbf{G}_4(\mathbf{G}_4^T\mathbf{Q}_{\mathbf{d}}^{-1}\mathbf{G}_4 + \bar{\mathbf{Q}}_{\dot{\boldsymbol{\varphi}}}^{-1})^{-1}\mathbf{G}_4^T\mathbf{Q}_{\mathbf{d}}^{-1}\mathbf{G}_3,\end{aligned} \tag{41}$$

where

$$\mathbf{G}_3 = \mathbf{B}_{\mathbf{d}}^{-1}\mathbf{G}\mathbf{M}, \tag{42}$$

$$\mathbf{G}_4 = -\mathbf{B}_{\mathbf{d}}^{-1}\mathbf{B}_{\dot{\boldsymbol{\varphi}}}. \tag{43}$$

After performing trivial linear algebra operations in Appendix B, we demonstrate that $\mathbf{G}_3 = \boldsymbol{\nabla}_{\mathbf{d}^o\mathbf{u}_0}$ and $\mathbf{G}_4 = \boldsymbol{\nabla}_{\mathbf{d}^o\Delta\dot{\boldsymbol{\varphi}}}$. As a result, it can be demonstrated that

$$\mathrm{cov}(\hat{\mathbf{u}}_0) = \mathrm{CRLB}(\mathbf{u}_0) \tag{44}$$

when the higher-order noise terms are negligible.

C. Computational Complexity

The worst-case time complexity [35] for obtaining the ϵ-solution of an SDP problem is

$$\mathcal{O}(\max(N_c, N)^4 N^{1/2}\log(1/\epsilon)), \tag{45}$$

where ϵ indicates the accuracy of the solution. N_c is the number of semidefinite constraints, and N is the number of variables. From (21), we have seven unknown variables and four constraints for the proposed WSDR. The worst-case complexity of solving the QCQP problem using the convex-based method depends on the solution's accuracy instead of the number of measurements.

V. Simulation

In the simulation, we compare the proposed WSDR solution with the semidefinite programming relaxation (SDP-R) estimator [31], the efficient unique solution with weighted least-square refinement (EUS-WLSR) [27], the Euclidean distance matrix completion (EDMC) estimator [25], and the two-stage weighted least square (TSWLS) estimator derived in Appendix C. The average root-mean-square error (RMSE) of 10 randomly generated localization geometries is calculated to validate the performance of the proposed methods. The total number of ensemble runs for each geometry is 100. We place the UWB modules on the x-axis of the robot body frames at $\mathbf{s}_0 = [-0.2, 0]^T$ meters and $\mathbf{t}_0 = [-0.2, 0]^T$ meters. The state transition vectors and the initial relative pose are randomly selected for each geometry. The change of position and orientation will not be significant in a short period of time. In the simulation, the rotation angles between two consecutive timestamps are restricted to be less than 20^o. And the robots travel less than 0.5 meters within a single sampling period.

In practice, UWB module accuracy is affected by various factors, such as multi-path propagation, interference, and occlusions. UWB measurement noises at different timestamps are assumed to be independent with different noise power. In the simulation, we choose a diagonal matrix with randomly selected diagonal elements within the interval of $[0.5\sigma_{\mathbf{d}}^2, 1.5\sigma_{\mathbf{d}}^2]$ as the covariance matrix of UWB measurements.

The state transition errors between two consecutive timestamps are IID. The 3×3 covariance matrices of the state transition errors are

$$\mathbf{Q}_{\dot{\boldsymbol{v}}} = \begin{bmatrix}\sigma^2_{\dot{\alpha}} & \mathbf{0}^T \\ \mathbf{0} & \mathbf{Q}_{\dot{\mathbf{a}}}\end{bmatrix}, \quad \mathbf{Q}_{\dot{\boldsymbol{\omega}}} = \begin{bmatrix}\sigma^2_{\dot{\beta}} & \mathbf{0}^T \\ \mathbf{0} & \mathbf{Q}_{\dot{\mathbf{b}}}\end{bmatrix}. \tag{46}$$

The first diagonal elements in $\mathbf{Q}_{\dot{\boldsymbol{v}}}$ and $\mathbf{Q}_{\dot{\boldsymbol{\omega}}}$ are the variances of the rotation angles. The bottom-right blocks of the covariance matrices correspond to the uncertainties of the translation vectors. Although the covariance matrices $\mathbf{Q}_{\mathbf{d}}$, $\mathbf{Q}_{\dot{\boldsymbol{v}}}$ and $\mathbf{Q}_{\dot{\boldsymbol{\omega}}}$ are diagonal in the simulation, the proposed algorithms can cope with the non-diagonal covariance matrices without further modification.

Note that the angle unit is degree, and the range unit is meter. Fig. 3 examines RMSE of the proposed relative localization solution when the noise power of the state transition error is fixed at $\sigma_{\dot{\alpha}} = \sigma_{\dot{\beta}} = 0.1$ degrees and $\sqrt{\mathrm{tr}(\mathbf{Q}_{\dot{\mathbf{a}}})} = \sqrt{\mathrm{tr}(\mathbf{Q}_{\dot{\mathbf{b}}})} = 0.01$ meters. We compare the RMSE of WSDR with the RMSEs of the comparison methods and the CRLB as the UWB measurement noise increases. The RMSE of TSWLS and WSDR achieve the CRLB performance when the UWB measurement noise is small. When the $\sigma_{\mathbf{d}}$ increases to 0.032 meters, TSWLS starts to diverge from the CRLB. The ranging accuracy of commercial UWB modules available in the market is 0.1 meters. Thus, TSWLS is not the best choice for the relative pose estimation using UWB modules. SDP-R does not reach the CRLB performance because the statistical property of the state transition vectors and the UWB measurements are not fully exploited. The RMSEs of EUS-WLSR and EDMC are dominated by the failed instance because the success rates of EUS-WLSR and EDMC are low. WSDR produces the smallest RMSE over the entire range of the noise power we examined. The RMSE of WSDR stays with the CRLB until $\sigma_{\mathbf{d}}$ increases to 0.1 meters.

In Fig. 4 and 5, the UWB measurement noise power is fixed to $\sigma_{\mathbf{d}} = 0.1$ meters. We examine the performance of the proposed solutions with increasing odometry error. In Fig. 4, $\sigma_{\dot{\alpha}}$ and $\sigma_{\dot{\beta}}$ increases while $\sqrt{\mathrm{tr}(\mathbf{Q}_{\dot{\mathbf{a}}})}$ and $\sqrt{\mathrm{tr}(\mathbf{Q}_{\dot{\mathbf{b}}})}$ is kept at 0.01 meters. In Fig. 5, we set $\sigma_{\dot{\alpha}}$ and $\sigma_{\dot{\beta}}$ to 0.1 degrees, and increase $\sqrt{\mathrm{tr}(\mathbf{Q}_{\dot{\mathbf{a}}})}$ and $\sqrt{\mathrm{tr}(\mathbf{Q}_{\dot{\mathbf{b}}})}$. In both Fig. 4 and Fig. 5, the RMSE of WSDR is slightly above the CRLB because the UWB measurement noise and the fixed part of the odometry uncertainties are not small. Nevertheless, SDP-R and WSDR are more robust than EUS-WLSR, EDMC, and TSWLS. Moreover, WSDR produces lower RMSE than SDP-R over all the noise

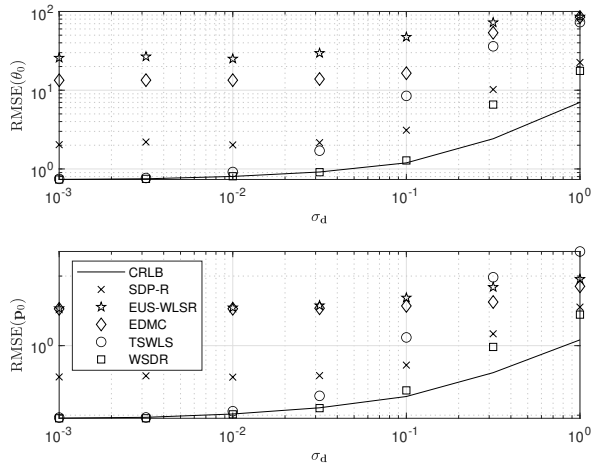

Fig. 3. RMSE of the relative pose estimation when $\sigma_\mathbf{d}$ increases.

levels examined.

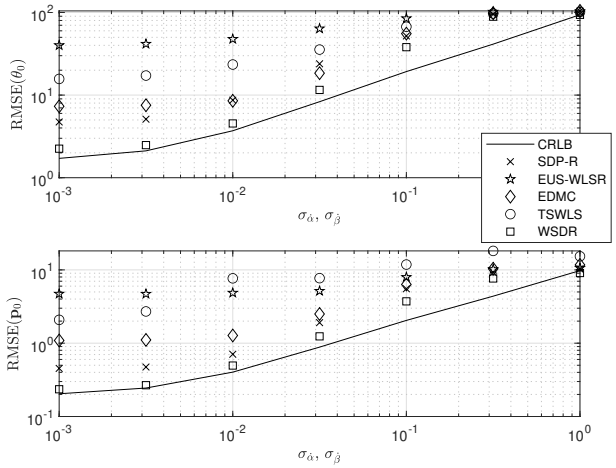

Fig. 4. RMSE of the relative pose estimation when $\sigma_{\dot\alpha}$ and $\sigma_{\dot\beta}$ increase.

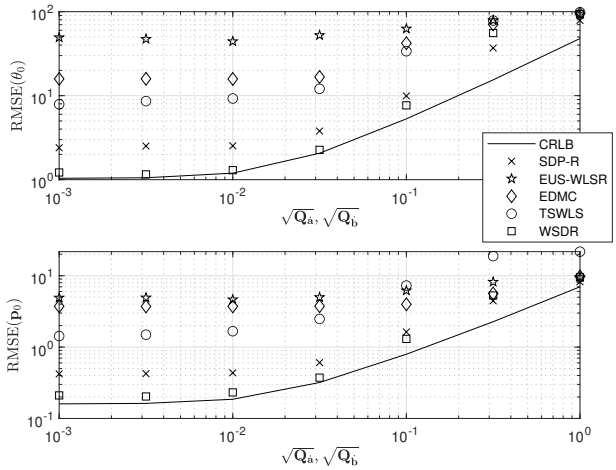

Fig. 5. RMSE of the relative pose estimation when $\sqrt{\mathrm{tr}(\mathbf{Q}_{\dot{\mathbf{a}}})}$ and $\sqrt{\mathrm{tr}(\mathbf{Q}_{\dot{\mathbf{b}}})}$ increase.

To understand how the number of measurements affects the localization performance, we fix $\sigma_\mathbf{d} = 0.1$ meters, $\sigma_{\dot\alpha} = \sigma_{\dot\beta} = 0.1$ degrees, and $\sqrt{\mathrm{tr}(\mathbf{Q}_{\dot{\mathbf{a}}})} = \sqrt{\mathrm{tr}(\mathbf{Q}_{\dot{\mathbf{b}}})} = 0.01$ meters. Fig. 6 shows an overall decreasing trend of the CRLB and the RMSEs as the number of measurements increases. Moreover, using additional measurements enhances the robustness of the proposed algorithms. The RMSE of WSDR overlaps with the CRLB when more than 50 measurements are used. SDP-R benefits less from additional measurements due to the cumulative errors in the positions of the UWB modules.

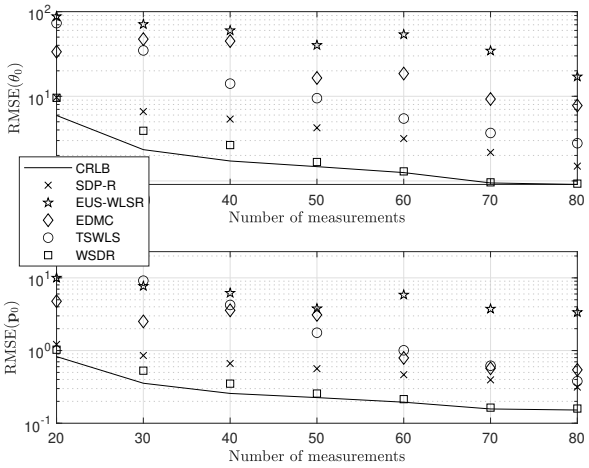

Fig. 6. RMSE of the relative pose estimation when the number of measurements increases.

Fig. 7 illustrates the randomly generated relative orientations and trajectories of four robots in a case study. Our goal is to estimate the relative pose of Robot 2, 3, and 4 in Robot 1's initial body frame. We test the localization geometry shown in Fig. 7 with 100 ensemble runs.

Fig. 8 shows the estimation performance of the relative orientation. The black dashed lines are the true value of the relative orientations. Each box chart displays the following information: the median, the quartiles, the minimum/maximum values, and the outliers. The variance of the EDMC is small. However, the median of the EDMC does not overlap with the true value for Robot 2 and Robot 3. EUS-WLSR generally gives a larger variance than the other methods because the efficient unique solution is calculated using only five range measurements. TSWLS diverges in some instances because it is sensitive to the UWB range measurement noise. As we mentioned, the convex-based SDP-R and WSDR perform more robustly than the other three estimators. In particular, the estimates obtained by WSDR lie around the true value and give the smallest variance.

Fig. 9(a) shows the overview performance in estimating the relative position of three robots. The other subplots are enlarged images of the uncertainty ellipses for different robots. The black circles indicate the true value of the relative positions. 90% of the estimates lie within the uncertainty ellipses of the respecting estimators. Fig. 9 shows that EDMC is a biased estimator with a small uncertainty ellipse. The uncertainty ellipses of EUS-WLSR and TSWLS are notably larger than the uncertainty ellipses of SDP-R and WSDR because of the failed instances. The uncertainty ellipses of SDP-R and WSDR cover small areas, and the averaged estimates lie close to the true positions. Although SDP-R and WSDR both perform well in this case study, it is worth noting that the variance of WSDR is lower than the variance of SDP-R.

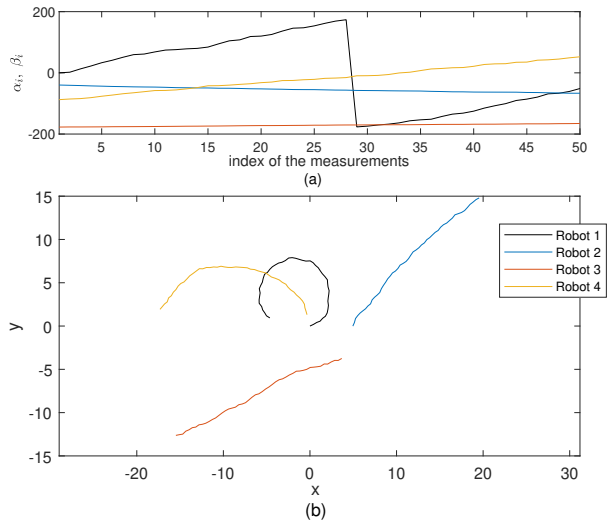

Fig. 7. (a) orientations and (b) trajectories of the robots in the case study.

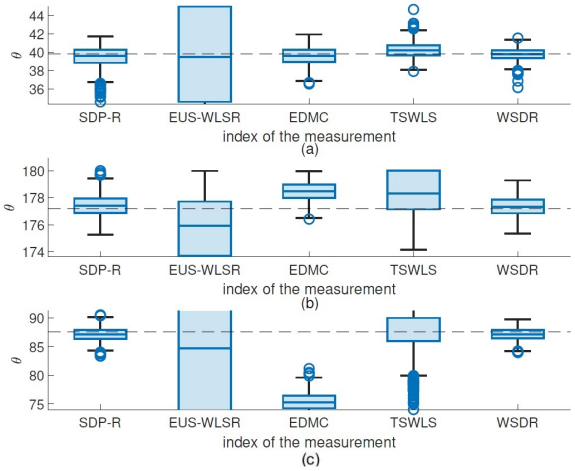

Fig. 8. A case study in estimating relative orientations of (a) Robot 2, (b) Robot 3, and (c) Robot 4.

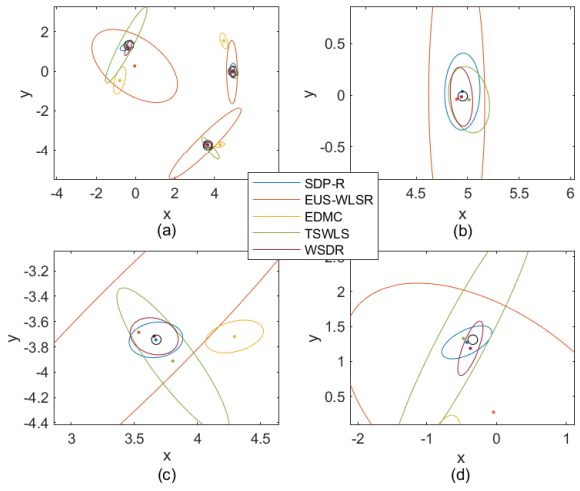

Fig. 9. (a) Overall performance in estimating robot relative position, and the enlarged plots of the uncertainty ellipses of (b) Robot 2, (c) Robot 3, and (d) Robot 4.

VI. Experiments

The real-world validation was conducted using two-wheeled robots (SPARKs) with IMU sensors and wheel encoders. Each robot equips one UWB module (Decawave DWM1000) measuring the inter-robot ranges. We test the proposed method on a 4×6 square meters field. A motion capture system (OptiTrack) with 16 calibrated cameras serves as the ground truth system, which captures the trajectory and orientation of four robots. Prior to the experiments, we collected several sets of distance and odometry measurements and compared them with OptiTrack results to compute the bias and covariance of the measurements. Fig. 10 shows our experimental environment, including the UWB modules in the red circles and four moving robots.

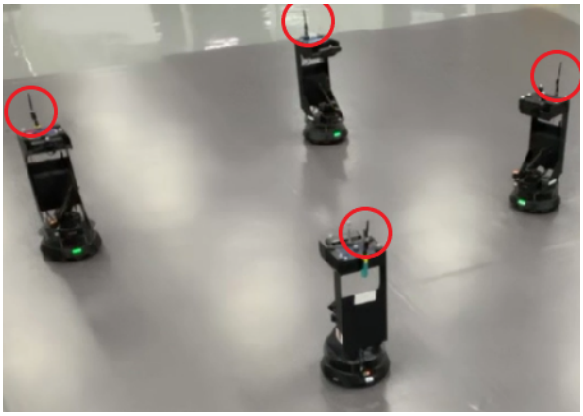

Fig. 10. Four robots move in the arena.

At each timestamp, we collect four moving robots' odometry and three range measurements between the reference robot and its neighbors. The sampling frequency is flexible because it depends on the network condition. The average sampling rate is 9.03 Hz in this experiment.

Fig. 11 illustrates the trajectories of the robots. The solid lines represent the robot poses measured by OptiTrack. The dashed lines are robot poses obtained by IMUs and wheel encoders in their initial body frames. Robot 1 moves in a uniform circular motion; Robot 2 runs at a constant linear speed; Robot 3 and 4 keep invariant orientations and make linear round trips at varying speeds. Bounding the robot orientation within $[-\pi, \pi]$ causes the sudden changes of the dashed orange line in Fig. 11(a). However, it won't affect the estimation and tracking results.

Fig. 12 shows the performance of robot relative localization and tracking in the laboratory environment. We denote Robot 1 as the reference robot. Orange, blue, and green represent the initial relative poses of Robot 2, 3, and 4, respectively. The squares, triangles, circles, crosses, plus signs, and Hexagrams represent the relative pose obtained by OptiTrack, TSWLS, WSDR, SDP-R, EUS-WLSR, and EDMC, respectively. The solid lines and dotted lines show the relative trajectories obtained from OptiTrack and odometry. The dashed lines and dash-dotted lines are the filtered result from the sliding window filter (SWF) and the extended Kalman filter (EKF) using the state transition model in (5a) and (5b). In Fig. 12, the initial estimates obtained by WSDR stay closest to their ground truth values.

Four datasets are collected to calculate the RMSEs in real-world validation. In each dataset, the localization algorithms are executed to estimate the relative pose of Robot 2, 3, and 4

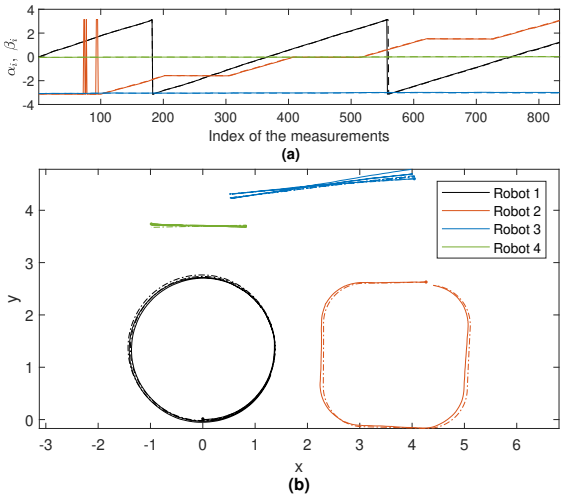

Fig. 11. Setup of real-world experiment. The solid lines represent the true trajectories captured by OptiTrack. The dashed lines show the trajectories obtained by odometry.

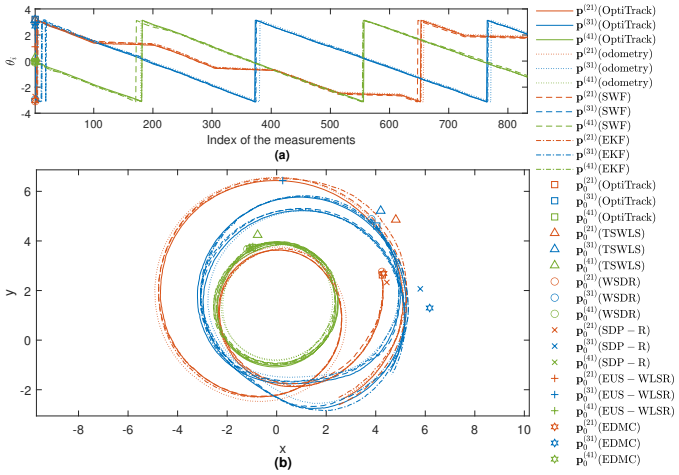

Fig. 12. Performance of the real-world experiment.

using the measurements from the first 100 frames. The results are listed in Table I. WSDR achieves the best accuracy in estimating both orientation and position, which are 3.97^o and 0.22 meters. The comparison methods produce large RMSEs because of the failed instances.

Accurate initial values of the relative poses are crucial for SWF and EKF. Thus, we initialize the position and orientation of the odometry, SWF, and EKF using the estimates obtained by WSDR. Fig. 13 shows the RMSEs of robot relative pose tracking. The purple line indicates the RMSE of robot tracking results relying on the odometry solely. SWF and EKF improve the accuracy of tracking when the frame index is over 200. Based on the results shown in Fig. 13, our strategy for determining the robots' relative poses at any given time is to initialize EKF with WSDR estimates and update the robots' relative poses using the odometry and UWB measurements from subsequent frames.

TABLE I
RMSE COMPARISON OF THE RELATIVE LOCALIZATION METHODS

	SDP-R	EUS -WLSR	EDMC	TSWLS	WSDR
RMSE(θ_0)	18.87^o	87.69^o	19.38^o	68.23^o	3.97^o
RMSE($\mathbf{p}_0$)	1.75 m	5.03 m	2.39 m	2.50 m	0.22 m

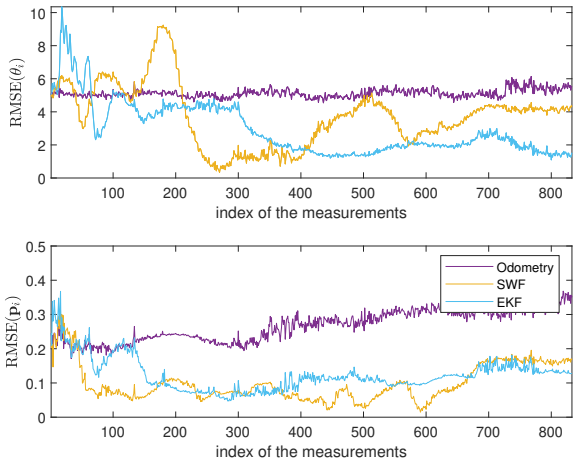

Fig. 13. RMSE of the robot relative pose tracking.

VII. Conclusion and Future Work

This study investigates the 2D robot relative localization problem using the inter-robot ranges measured by UWB modules when each robot operates under its local frame with an imperfect odometer. A novel formulation and a WSDR solution are developed to determine the initial robot relative pose. Performance analysis proves that WSDR achieves CRLB performance when the noise power is insignificant. Simulations and real-world experiments validate the performance of WSDR. Future work will focus on the multi-robot relative localization and tracking problem in 3D. For large-scale, low-cost MEMS-based multi-robot navigation systems, computing covariance matrices through the orthogonal projection principle [37], [38] is an attractive topic for future investigation because it reduces computation loads and improves the tracking performance.

VIII. Acknowledgment

The authors would like to thank the anonymous reviewers for providing valuable comments that have helped us to improve the quality of the paper. The authors would like to thank Cameron Mahon, who has assisted with the English language review.

Appendix A

In some cases, we are interested in estimating the current relative pose of the robots instead of the initial relative pose. To determine the relative pose of Robot 2 in $\mathcal{A}_M$ instead of $\mathcal{A}_0$, we compute the reverse transition vector is

$$\ddot{\boldsymbol{\upsilon}}_i = [-\dot{\alpha}_i, -\dot{\mathbf{a}}_i^T \mathbf{R}_{\dot{\alpha}_i}]^T. \tag{47}$$

The covariance of $\ddot{\boldsymbol{\upsilon}}_i$ is $\mathbf{Q}_{\ddot{\boldsymbol{\upsilon}}_i} = \boldsymbol{\nabla}_{\Delta\ddot{\boldsymbol{\upsilon}}_i \Delta\dot{\boldsymbol{\upsilon}}_i} \mathbf{Q}_{\dot{\boldsymbol{\upsilon}}} \boldsymbol{\nabla}^T_{\Delta\ddot{\boldsymbol{\upsilon}}_i \Delta\dot{\boldsymbol{\upsilon}}_i}$, where

$$\boldsymbol{\nabla}_{\Delta\ddot{\boldsymbol{\upsilon}}_i \Delta\dot{\boldsymbol{\upsilon}}_i} = \begin{bmatrix} -1 & \mathbf{0}^T \\ -\mathbf{R}'_{\dot{\alpha}_i^o} \dot{\mathbf{a}}_i^{o^T} & -\mathbf{R}_{\dot{\alpha}_i^o} \end{bmatrix}. \tag{48}$$

Since the reverse transition errors between any two timestamps are independent, the covariance of $\ddot{\boldsymbol{\upsilon}}$ is

$$\mathbf{Q}_{\ddot{\boldsymbol{\upsilon}}} = \text{blkdiag}(\mathbf{Q}_{\ddot{\boldsymbol{\upsilon}}_M}, \ldots, \mathbf{Q}_{\ddot{\boldsymbol{\upsilon}}_1}). \tag{49}$$

The reverse state transition vector of Robot 2 and its covariance matrix are computed following similar steps. With the reverse state transition vectors and the range measurements, $\mathbf{u}_M$ can be solved by applying WSDR directly.

APPENDIX B

Substituting (16), (33) and $\mathbf{B_d}$ into (42) yields

$$\begin{aligned}\mathbf{G}_3(i+1,1) &= (-\cos\theta_0(t^o_{ix}s^o_{iy} - t^o_{iy}s^o_{ix}) \\ &+ \sin\theta_0(t^o_{ix}s^o_{ix} + t^o_{iy}s^o_{iy}) + t^o_{ix}(p_{0y}\cos\theta_0 - p_{0x}\sin\theta_0) \\ &- t^o_{iy}(p_{0x}\cos\theta_0 + p_{0y}\sin\theta_0))/d_i = \boldsymbol{\rho}_i^{oT}\mathbf{R}'_{\theta_0}\mathbf{t}_i. \end{aligned} \tag{50}$$

$$\mathbf{G}_3(i,2:3) = \frac{(\mathbf{R}_{\theta_0}\mathbf{t}_i + \mathbf{p}_0 - \mathbf{s}_i)^T}{d_i} = \boldsymbol{\rho}_i^{oT}. \tag{51}$$

From (50) and (51), we prove that $\mathbf{G}_3 = \boldsymbol{\nabla}_{\mathbf{d}^o\mathbf{u}}$.

Combining $\mathbf{B_d}$, (18a) and (18b) gives

$$\mathbf{B_d}^{-1}\mathbf{B_s} = -\boldsymbol{\nabla}_{\mathbf{d}^o\mathbf{s}^o}, \quad \mathbf{B_d}^{-1}\mathbf{B_t} = -\boldsymbol{\nabla}_{\mathbf{d}^o\mathbf{t}^o}. \tag{52}$$

Combining (39), (43), and (52), we have

$$\mathbf{G}_4 = [\boldsymbol{\nabla}_{\mathbf{d}^o\mathbf{s}^o}\boldsymbol{\nabla}_{\mathbf{s}^o\boldsymbol{v}^o}\boldsymbol{\nabla}_{\boldsymbol{v}^o\Delta\dot{\boldsymbol{v}}}, \boldsymbol{\nabla}_{\mathbf{d}^o\mathbf{t}^o}\boldsymbol{\nabla}_{\mathbf{t}^o\boldsymbol{\omega}^o}\boldsymbol{\nabla}_{\boldsymbol{\omega}^o\Delta\dot{\boldsymbol{\omega}}}] = \boldsymbol{\nabla}_{\mathbf{d}^o\Delta\dot{\boldsymbol{\varphi}}}. \tag{53}$$

APPENDIX C

TSWLS is derived to determine relative robot pose at low computational cost. In the first stage, we ignore the relationships between the elements of $\mathbf{v}$ and solve (15) as an unconstrained problem using the weighted least square estimator. The solution of the first stage is

$$\check{\mathbf{v}} = (\mathbf{G}^T\mathbf{W}\mathbf{G})^{-1}\mathbf{G}^T\mathbf{W}\mathbf{h}, \tag{54}$$

The second stage of the TSWLS method aims to refine the relative pose estimate by exploring the relationships among the elements in the augmented unknown vector $\mathbf{v}$. We use the output of the first stage as the input of the second stage. The estimation error of the first stage becomes the input noise of the second stage. Denote the unknown parameter vector of the second stage as $\mathbf{v}_2 = [\cos\theta_0^2, \mathbf{p}_0^T]^T$. Expressing $\check{\mathbf{v}}$ by $\mathbf{v}_2$ and collecting all error terms on one side gives

$$\mathbf{h}_2 - \mathbf{G}_2\mathbf{v}_2 = \mathbf{B}_2\Delta\mathbf{v} \tag{55}$$

where

$$\mathbf{G}_2 = \begin{bmatrix} 1 & 1 & 0 & 0 & 0 & 0 & 0 \\ 0 & 0 & 1 & 0 & \check{\mathbf{v}}(2) & -\check{\mathbf{v}}(1) & \check{\mathbf{v}}(3) \\ 0 & 0 & 0 & 1 & \check{\mathbf{v}}(1) & \check{\mathbf{v}}(2) & \check{\mathbf{v}}(4) \end{bmatrix}^T, \tag{56}$$

$$\mathbf{h}_2 = [1 - \check{\mathbf{v}}(1)^2, \check{\mathbf{v}}(2)^2, \check{\mathbf{v}}(3:7)^T]^T. \tag{57}$$

The weighting matrix of the second stage is

$$\mathbf{W}_2 = (\mathbf{B}_2\mathrm{cov}(\check{\mathbf{v}})\mathbf{B}_2{}^T)^{-1} = \mathbf{B}_2^{-T}\mathbf{G}^T\mathbf{W}\mathbf{G}\mathbf{B}_2^{-1}, \tag{58}$$

where $\mathrm{cov}(\check{\mathbf{v}})$ is the covariance matrix of the estimation error of the first stage result. Replacing $\mathbf{v}_2(2:3)$ with $\mathbf{v}(3:4)$ in $\mathbf{B}_2$ gives

$$\mathbf{B}_2 = \begin{bmatrix} -2\mathbf{v}(1) & 0 & 0 & 0 & 0 & 0 & 0 \\ 0 & 2\mathbf{v}(2) & 0 & 0 & 0 & 0 & 0 \\ 0 & 0 & 1 & 0 & 0 & 0 & 0 \\ 0 & 0 & 0 & 1 & 0 & 0 & 0 \\ -\mathbf{v}(4) & -\mathbf{v}(3) & 0 & 0 & 1 & 0 & 0 \\ \mathbf{v}(3) & -\mathbf{v}(4) & 0 & 0 & 0 & 1 & 0 \\ 0 & 0 & -\mathbf{v}(3) & -\mathbf{v}(4) & 0 & 0 & 1 \end{bmatrix}. \tag{59}$$

In practice, $\mathbf{B}_2$ is constructed using the first stage estimate $\check{\mathbf{v}}$ instead of its true value. The WLS solution of the second stage is

$$\check{\mathbf{v}}_2 = (\mathbf{G}_2^T\mathbf{W}_2\mathbf{G}_2)^{-1}\mathbf{G}_2^T\mathbf{W}_2\mathbf{h}_2. \tag{60}$$

Because the value of $\cos^2\theta_0$, $\cos^2(-\theta_0)$, $\cos^2(\pi-\theta_0)$ and $\cos^2(-\pi+\theta_0)$ are equal, estimating $\cos^2\theta_0$ instead of $\sin\theta_0$ and $\cos\theta_0$ introduces ambiguities in the rotation angle. We utilize the sign of the $\check{\mathbf{v}}$ to restore the information loss. Denote $\mathbf{l} = \mathrm{sgn}(\check{\mathbf{v}})$ as the sign of $\check{\mathbf{v}}$, the final result of the TSWLS estimator is given by

$$\check{\mathbf{u}}_0 = \begin{bmatrix} \mathrm{angle}\left(\mathbf{l}(2)\sqrt{\check{\mathbf{v}}_2(1)} + \mathbf{l}(1)\sqrt{\check{\mathbf{v}}_2(1)-1}\right) \\ \check{\mathbf{v}}_2(2:3) \end{bmatrix}. \tag{61}$$

The closed-form TSWLS estimator is computationally more efficient than the convex-based methods. However, TSWLS does not guarantee that $\mathbf{v}_1(1)$, $\mathbf{v}_1(2)$, and $\mathbf{v}_2(1)$ take values between 0 and 1. Furthermore, we ignore the higher-order noise term in both stages of TSWLS. As a result, TSWLS will diverge earlier than the convex-based method when the range measurement noise and the odometry uncertainties become significant.

REFERENCES

[1] M. Zhang, X. Zuo, Y. Chen, Y. Liu, and M. Li, "Pose estimation for ground robots: on manifold representation, integration, reparameterization, and optimization," *IEEE Trans. Robot.*, vol. 37, no. 4, pp. 1081-1099, Aug. 2021.

[2] H. M. Cho, H. Jo, and E. Kim, "SP-SLAM: surfel-point simultaneous localization and mapping," *IEEE/ASME Trans. Mechatron.*, early access, Oct. 2021, doi: 10.1109/TMECH.2021.3118719.

[3] P. Doostdar, J. Keighobadi, and M. A. Hamed, "INS/GNSS integration using recurrent fuzzy wavelet neural networks," *GPS Solut.*, vol. 24, no. 29, pp. 1-15, Dec. 2019.

[4] S. Safavi and U. A. Khan, "An opportunistic linear–convex algorithm for localization in mobile robot networks," *IEEE Trans. Robot.*, vol. 33, no. 4, pp. 875-888, Aug. 2017.

[5] S. Zhang, J. Shan, and Y. Liu, "Variational Bayesian estimator for mobile robot localization with unknown noise covariance," *IEEE/ASME Trans. Mechatron.*, early access, Apr. 2022, doi:10.1109/TMECH.2022.3161591.

[6] J. Wang, Z. Meng, and L. Wang, "A UPF-PS SLAM algorithm for indoor mobile robot with nonGaussian detection model," *IEEE/ASME Trans. Mechatron.*, vol. 27, no. 1, pp. 1-11, Feb. 2022.

[7] M. Li, T. L. Lam, and Z. Sun, "3-D inter-robot relative localization via semidefinite optimization,"*IEEE Robot. Autom. Lett.*, vol. 7, no. 4, pp. 10081-10088, Jul. 2022.

[8] Q. Hu and C. Jiang, "Relative stereovision-based navigation for noncooperative spacecraft via feature extraction," *IEEE/ASME Trans. Mechatron.*, early access, Dec. 2021, doi: 10.1109/TMECH.2021.3128402.

[9] T. Ibuki, S. Wilson, J. Yamauchi, M. Fujita, and M. Egerstedt, "Optimization-based distributed flocking control for multiple rigid bodies," *IEEE Robot. Autom. Lett.*, vol. 5, no. 2, pp. 1891-1898, Apr. 2020.

[10] K. M. Kabore and S. Güler, "Distributed formation control of drones with onboard perception," *IEEE/ASME Trans. Mechatron.*, early access, Sept. 2021, doi: 10.1109/TMECH.2021.3110660.

[11] T. Ziegler, M. Karrer, P. Schmuck, and M. Chli, "Distributed formation estimation via pairwise distance measurements," *IEEE Robot. Autom. Lett.*, vol. 6, no. 2, pp. 3017-3024, Apr. 2021.

[12] G. Liang, H. Luo, M. Li, H. Qian, and T. L. Lam, "FreeBOT: a freeform modular self-reconfigurable robot with arbitrary connection point - design and implementation," *2020 IEEE/RSJ Int. Conf. Intell. Robots Syst. (IROS)*, Las Vegas, Nevada, Oct. 2020, pp. 6506-6513.

[13] A. Bhattacharjee, Y. Lu, A. T. Becker, and M. Kim, "Magnetically controlled modular cubes with reconfigurable self-assembly and disassembly," *IEEE Trans. Robot.*, vol. 38, no. 3, pp. 1793-1805, Jun. 2022.

[14] T. Ran, L. Yuan, J. Zhang, L. He, R. Huang, and J. Mei, "Not only look but infer: multiple hypothesis clustering of data association inference for semantic SLAM," *IEEE Trans. Instrum. Meas.*, vol. 70, pp. 1-9, Apr. 2021.

[15] Y. Wang, K. C. Ho, and L. Huang, "Room geometry estimation using the multipath delays," *IEEE Signal Process. Lett.*, vol. 28, pp. 1380-1384, Jun. 2021.

[16] A. Franchi, G. Oriolo, and P. Stegagno, "Mutual localization in multi-robot systems using anonymous relative measurements." *Int. J. Rob. Res.*, vol. 32, no. 11, pp. 1302-1322, Sept. 2013.

[17] P. Stegagno, M. Cognetti, G. Oriolo, H. H. Bülthoff, and A. Franchi, "Ground and aerial mutual localization using anonymous relative-bearing measurements," *IEEE Trans. Robot.*, vol. 32, no. 5, pp. 1133-1151, Oct. 2016.

[18] C. C. Cossette, M. Shalaby, D. Saussié, J. R. Forbes, and J. Le Ny, "Relative position estimation between two UWB devices with IMUs," *IEEE Robot. Autom. Lett.*, vol. 6, no. 3, pp. 4313-4320, Jul. 2021.

[19] J. Jiang, G. Wang, and K. C. Ho, "Sensor network-based rigid body localization via semi-definite relaxation using arrival time and Doppler measurements," *IEEE Trans. Wireless Commun.*, vol. 18, no. 2, pp. 1011-1025, Feb. 2019.

[20] Y. Wang, G. Wang, S. Chen, K. C. Ho, and L. Huang, "An investigation and solution of angle based rigid body localization," *IEEE Trans. Signal Process.*, vol. 68, pp. 5457-5472, Sept. 2020.

[21] A. I. Mourikis and S. I. Roumeliotis, "Performance analysis of multirobot Cooperative localization," *IEEE Trans. Robot.*, vol. 22, no. 4, pp. 666-681, Aug. 2006.

[22] S. Güler, M. Abdelkader, and J. S. Shamma, "Peer-to-peer relative localization of aerial robots with ultrawideband sensors," *IEEE Trans. Control Syst. Technol.*, vol. 29, no. 5, pp. 1981-1996, Sept. 2021.

[23] M. Shalaby, C. C. Cossette, J. R. Forbes, and J. Le Ny, "Relative position estimation in multi-agent systems using attitude-coupled range measurements," *IEEE Robot. Autom. Lett.*, vol. 6, no. 3, pp. 4955-4961, Jul. 2021.

[24] C. -C. Peng, J. -J. Huang, and H. -Y. Lee, "Design of an embedded icosahedron mechatronics for robust iterative IMU calibration," *IEEE/ASME Trans. Mechatron.*, early access, Jul. 2021, doi: 10.1109/TMECH.2021.3099119.

[25] I. Dokmanic, R. Parhizkar, J. Ranieri, and M. Vetterli, "Euclidean distance matrices: essential theory, algorithms, and applications," *IEEE Signal Process. Mag.*, vol. 32, no. 6, pp. 12-30, Nov. 2015.

[26] M. Pacholska, F. Dümbgen, and A. Scholefield, "Relax and recover: guaranteed range-only continuous localization," *IEEE Robot. Autom. Lett.*, vol. 5, no. 2, pp. 2248-2255, Apr. 2020.

[27] X. S. Zhou and S. I. Roumeliotis, "Robot-to-robot relative pose estimation from range measurements," *IEEE Trans. Robot.*, vol. 24, no. 6, pp. 1379-1393, Dec. 2008.

[28] X. S. Zhou and S. I. Roumeliotis, "Determining the robot-to-robot 3D relative pose using combinations of range and bearing measurements: 14 minimal problems and closed-form solutions to three of them," in *Proc. IEEE/RSJ Int. Conf. Intell. Robots Syst.*, Taipei, Taiwan, Oct. 2010, pp. 2983-2990.

[29] X. S. Zhou and S. I. Roumeliotis, "Determining the robot-to-robot 3D relative pose using combinations of range and bearing measurements (Part II)," in *Proc. IEEE Int. Conf. Robot. Autom.*, Shanghai, China, May 2011, pp. 4736-4743.

[30] N. Trawny and S. I. Roumeliotis, "On the global optimum of planar, range-based robot-to-robot relative pose estimation," in *Proc. IEEE Int. Conf. Robot. and Autom.*, Anchorage, AK, May 2010, pp. 3200-3206.

[31] M. Li, G. Liang, H. Luo, H. Qian, and T. L. Lam, "Robot-to-robot relative pose estimation based on semidefinite relaxation optimization," in *Proc. IEEE/RSJ Int. Conf. Intell. Robots Syst.*, Las Vegas, Nevada, Oct. 2020, pp. 4491-4498.

[32] N. Trawny, X. S. Zhou, K. X. Zhou, and S. I. Roumeliotis, "3D relative pose estimation from distance-only measurements," in *Proc. IEEE/RSJ Int. Conf. Intell. Robots Syst.*, San Diego, California, Oct. 2007, pp. 1071-1078.

[33] S. M. Kay, *Fundamentals of Statistical Signal Processing: Estimation Theory*. Englewood Cliffs, NJ, USA: Prentice-Hall, 1993.

[34] T. D. Barfoot and P. T. Furgale, "Associating uncertainty with three-dimensional poses for use in estimation problems," *IEEE Trans. Robot.*, vol. 30, no. 3, pp. 679-693, Jun. 2014.

[35] Z. Q. Luo, W. K. Ma, A. M. C. So, Y. Ye, and S. Zhang, "Semidefinite relaxation of quadratic optimization problems," *IEEE Signal Process. Mag.*, vol. 27, no. 3, pp. 20-34, May 2010.

[36] M. Grant and S. Boyd. *CVX: MATLAB Software for Disciplined Convex Programming, Version 1.21*. [Online]. Available: http://cvxr.com/cvx

[37] H. Nourmohammadi and J. Keighobadi, "Decentralized INS/GNSS system with MEMS-grade inertial sensors using QR-factorized CKF," *IEEE Sensors J*, vol. 17, no. 11, pp. 3278-3287, Jun. 2017.

[38] J. Keighobadi, J. Faraji, F. J. -Sharifi, and M. A. Hamed, "Design and experimental evaluation of block-pulse functions and Legendre polynomials observer for attitude-heading reference system," *ISA Trans.*, vol. 116, pp. 232-244, Oct. 2021.

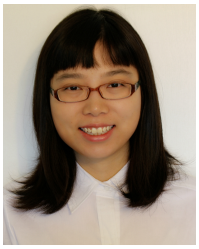

Yue Wang received her M.S. degree in electrical and computer engineering and her Ph.D. degree in electrical and computer engineering from the University of Missouri, Columbia, MO, USA, in 2011 and 2017, respectively. She is currently an Associate Research Scientist at the Shenzhen Institute of Artificial intelligence and Robotics for Society. Her research interests include target localization and sensor array processing.

Muhan Lin was born in Fujian Province, China in 2001. She is a junior computer engineering student at the Chinese University of Hong Kong (Shenzhen). She currently serves as a researcher at Shenzhen Institute of Artificial Intelligence and Robotics for Society and the Air Lab at Carnegie Mellon University. Her research interest lies in multi-robot cooperation and multi-sensor fusion.

Xinyi Xie is currently an undergraduate student of Computer Science at the Chinese University of Hong Kong, Shenzhen. She is also an undergraduate researcher at the Shenzhen Institute of Artificial intelligence and Robotics for Society. Her research interests are in the area of human-machine interaction and robotics.

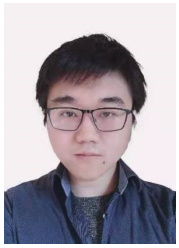

Yuan Gao received his M.S. degree in Machine Learning and Algorithms from the University of Helsinki, Finland in 2016 and received a Ph.D. degree from the Department of Information Technology, Uppsala University, Sweden, in 2020. He is currently an Assistant Research Scientist at the Shenzhen Institute of Artificial intelligence and Robotics for Society. His research interests include machine behaviour analysis, reinforcement learning, robotics, and general machine learning.

Fuqin Deng received his Ph.D. degree in electrical and electronic engineering from the University of Hong Kong, in 2014. He is currently a distinguished professor with School of Intelligent Manufacturing, Wuyi University. And he is also a research scientist with Shenzhen Institute of Artificial Intelligence and Robotics for Society (AIRS). His research interests include multi-robot systems, machine learning and machine vision applications.

Tin Lun Lam (Senior Member, IEEE) received the Ph.D. degree from the Chinese University of Hong Kong, Hong Kong, in 2010. He is an Assistant Professor with the Chinese University of Hong Kong, Shenzhen, China, and the Director of Center for the Intelligent Robots, Shenzhen Institute of Artificial Intelligence and Robotics for Society. His research interests include multi-robot systems, field robotics, and collaborative robotics.